condensed matter

MDPI

Article

Boron Concentration Induced Co-Ta-B Composite Formation Observed in the Transition from Metallic to Covalent Glasses

Simon Evertz [1,*], Stephan Prünte [1], Lena Patterer [1], Amalraj Marshal [1], Damian M. Holzapfel [1], Alexander Schökel [2], Marcus Hans [1], Daniel Primetzhofer [3] and Jochen M. Schneider [1]

1 Materials Chemistry, RWTH Aachen University, Kopernikusstr. 10, 52074 Aachen, Germany; pruente@mch.rwth-aachen.de (S.P.); patterer@mch.rwth-aachen.de (L.P.); amalraj@mch.rwth-aachen.de (A.M.); holzapfel@mch.rwth-aachen.de (D.M.H.); hans@mch.rwth-aachen.de (M.H.); schneider@mch.rwth-aachen.de (J.M.S.)

2 Deutsches Elektronen-Synchrotron DESY, FS-PE, Notkestr. 85, 22602 Hamburg, Germany; alexander.schoekel@desy.de

3 Department of Physics and Astronomy, Uppsala University, S-75120 Uppsala, Sweden; daniel.primetzhofer@physics.uu.se

* Correspondence: evertz@mch.rwth-aachen.de

Received: 12 February 2020; Accepted: 16 March 2020; Published: 18 March 2020

Abstract: Due to their unique property combination of high strength and toughness, metallic glasses are promising materials for structural applications. As the behaviour of metallic glasses depends on the electronic structure which in turn is defined by chemical composition, we systematically investigate the influence of B concentration on glass transition, topology, magnetism, and bonding for B concentrations x = 2 to 92 at.% in the $(Co_{6.8\pm3.9}Ta)_{100-x}B_x$ system. From an electronic structure and coordination point of view, the B concentration range is divided into three regions: Below 39 ± 5 at.% B, the material is a metallic glass due to the dominance of metallic bonds. Above 69 ± 6 at.%, the presence of an icosahedra-like B network is observed. As the B concentration is increased above 39 ± 5 at.%, the B network evolves while the metallic coordination of the material decreases until the B concentration of 67 ± 5 at.% is reached. Hence, a composite is formed. It is evident that, based on the B concentration, the ratio of metallic bonding to icosahedral bonding in the composite can be controlled. It is proposed that, by tuning the coordination in the composite region, glassy materials with defined plasticity and processability can be designed.

Keywords: metallic glass; composite; metalloid network; bonding

1. Introduction

Metallic glasses are promising materials for structural applications due to their unique property combination of high yield strength and fracture toughness [1–5]. While they are capable of plastic deformation at the microscale [5], the glass forming ability (GFA) poses often formidable challenges for both, processing and application [6]. Alloying with metalloids such as B can enhance the GFA in metallic glasses [3,7,8]. Co-B based metallic glasses with boron concentrations in the range of 35 at.% have been reported to exhibit yield strengths larger than 5000 MPa [9,10]. With increasing B concentrations up to 50 at.%, the fracture strength reaches values up to 11,000 MPa [11]. Simultaneously, between 28 and 50 at.% B the reduced Young's modulus increases from 280 to 345 GPa, hardness from 10 to 13 GPa, and fracture toughness from 2.5 to 6 $MPa{\cdot}m^{0.5}$ [11]. Based on ab initio calculations, a stiffness of 263 GPa is predicted for $Co_{33.0}Ta_{3.5}B_{63.5}$ [12]. On the other hand, amorphous borides with B concentrations >90 at.% form icosahedra-like B networks [13] and are reported to be ultra-hard [14,15], exhibit low friction due to self-lubrication [15], and show catalytic properties [16]. However, those

covalent borides exhibit brittle behaviour [13] in contrast to metallic glasses. For Co-Ta-B, the range of B concentration for which the transition from metallic glass to covalent glasses occurs has not been studied. Furthermore, the impact of B additions on the electronic structure and properties of Co-Ta-B has not been investigated systematically. Hence, to identify and to rationalise the composition induced changes in the electronic structure of metallic and covalent Co-Ta-B glasses as well as within their transition regime, we vary the B concentration of $(Co_{6.8\pm3.9}Ta)_{100-x}B_x$ supercells between x = 2 and 92 at.% in ab initio calculations and between x = 22 and 85 at.% in experimental samples. Specifically, we probe the B concentration induced changes in glass transition, topology, magnetisation, and bonding by ab initio calculations as well as high energy X-ray scattering, magnetometry, and X-ray photoelectron spectroscopy. Thereby, we reveal that the transition from a metallic to a covalent glass is associated with the formation of a composite.

2. Methods

2.1. Theoretical Methods

Density-functional-theory (DFT) [17] based ab initio molecular dynamic calculations were conducted on a supercell containing 115 atoms of composition $(Co_{6.8\pm3.9}Ta)_{100-x}B_x$ (x = 2 to 92 at.%). Following the modelling routine for metallic glasses developed by Hostert et al. [18], the supercell was heated up to 4000 K for 400 fs in an NVT ensemble and subsequently quenched to 0 K by geometry relaxation using the openMX code (version 3.8) [19,20]. Electronic potentials with the general gradient approximation were employed [21]. The following basis functions were applied: Co5.5-s2p1d1, Ta7.0-s2p1d1f1 and B4.5-s2p2. The first symbol designates the chemical element followed the cutoff-radius. The primitive orbitals are defined by the last set of symbols. A k-grid of 1x1x1 and a cutoff-radius of 150 Ry were used. The temperature was controlled by scaling of velocities. After quenching to 0 K, the volume was relaxed employing the Vienna Ab initio Simulation Package (VASP) [22,23] with projector augmented-wave potentials [23,24] using the Perdew-Burke-Ernzerhof functional [21] and integration over the Brillouin zone on a 3x3x3 Monkhorst-Pack k-grid [25]. The iteration cycle of heating-quenching-volume relaxation was repeated until the volume change was smaller than 2%. To calculate the pair distribution function G(r) from the atomic positions, the relaxed structure was hold at 300 K for 200 fs. G(r) was averaged over time. The crystal orbital overlap populations (COOP) [26] and crystal orbital Hamilton populations (COHP) [27] were calculated using the LOBSTER code (version 3.2.0) [28–30].

2.2. Experimental Methods

Magnetron sputtering was utilized to synthesize $(Co_{6.8\pm3.9}Ta)_{100-x}B_x$ (x = 22 to 85 at.%) thin films on Si, NaCl, and polyimide substrates for the characterization of chemistry, magnetic, and binding properties; glass transition; and topology, respectively. Therefore, an ultra-high vacuum combinatorial growth system [31] with a base pressure lower than 2×10^{-8} Pa and a target-to-substrate distance of 10 cm was employed. Floating substrate potential and non-intentional heating were used. For depositions on Si and polyimide substrates, the substrate was not rotated to obtain combinatorial samples. For depositions on NaCl, substrate rotation was used to obtain homogeneous films. The NaCl substrate was subsequently dissolved in deionized water. The resulting thin film flakes were cleaned in isopropanol and acetone for usage in in situ heating high energy X-ray scattering experiments. Up to three 2-inch B targets with a purity of 99.9% and one 2-inch $Co_{88}Ta_{12}$ target with 99.9% purity were used. The working gas during deposition was Ar (purity 6.0) with a pressure of 0.4 Pa. The B targets were sputtered in RF mode with up to 10.2 Wcm^{-2}, while the CoTa target was sputtered in DC mode with up to 1.5 Wcm^{-2}.

The chemical composition was determined using standard-based energy dispersive X-ray spectroscopy with a Bruker Quantax75 EDS system in a Hitachi TM4000plus scanning electron microscope. The EDX measurements were calibrated with a $Co_{71}Ta_6B_{23}$ thin film which was characterized by ion

beam analysis using time-of-flight elastic recoil detection analysis (ToF-ERDA) at the tandem accelerator laboratory of Uppsala University. Recoils were generated by $^{127}I^{8+}$ primary ions with a kinetic energy of 36 MeV. The detector telescope, consisting of thin carbon foils for the ToF [32] as well as a gas ionization detection system [33], was situated at an angle of 45° with respect to the primary ions and both the incidence as well as exit angles were 22.5° with respect to the specimen surface. Time and energy coincidence spectra were converted into a depth profile using the CONTES software package [34]. The O concentration of the $Co_{71}Ta_6B_{23}$ thin film was <1 at.%. Meanwhile, the statistical uncertainty of the concentration was with 2% relative deviation maximum for B and maximum systematic uncertainties of 10% relative deviation are assumed due to uncertainties of the specific energy loss of primary ions and recoiled species.

High energy X-ray scattering was carried out at beamline P02.1 [35] of the PETRA III electron storage ring at Deutsches Elektronen-Synchrotron (DESY), Hamburg, Germany, utilizing X-rays with a wavelength of 0.20701 Å. To measure the topology along the CoTa-B compositional gradients, samples deposited on polyimide were measured [31]. To determine the structural changes and the glass transition temperature T_g, powder samples sealed in fused silica capillaries under Ar atmosphere were heated in situ by a Si_3N_4 heating element (Bach RC GmbH) to temperatures up to 1400 K with a heating rate of 15 K/min. Data were collected with a Perkin Elmer XRD 1621 plate detector and integrated by the FIT2D software [36–38]. The background-corrected data were used to calculate the structure factor as well as the pair distribution function G(r) by a fast Fourier transformation implemented in the PDFgetX3 software package [39].

Binding energies were measured by X-ray photoelectron spectroscopy (XPS) in a Kratos Analytical Axis Supra. Al Kα radiation (photon energy 1.4866 keV) was employed. The sample was deposited immediately prior to the XPS measurement. However, due to the contact to ambient atmosphere during sample transfer (~15 min), the surface has already been oxidized. To remove the oxide, the sample was etched using an Ar^+ ions with an energy of 500 eV for 120 s. The binding energy was corrected for charging by using the C 1s peak at 285 eV for calibration. CasaXPS software was utilised to analyse the acquired spectra employing Shirley backgrounds. The B 1s peak was fitted with a mixed Gauss-Lorentz peak (30/70) and the Co 2p signal was fitted according to Biesinger et al. [40]. The saturation magnetization was measured at room temperature using the Vibrating Sample Magnetometer (VSM) option at a physical property measurement system (PPMS) from Quantum Design employing a maximum magnetic field of 2 T.

3. Results and Discussion

3.1. Glass Transition

As a first indicator for differences between high and low boron concentration regimes, the glass transition temperature T_g as an integral measure for the structure of a glass is considered. Table 1 lists the glass transition temperatures obtained by measuring average atomic volume changes by high energy X-ray scattering (Supplementary Figure S1) for $(Co_{6.8\pm3.9}Ta)_{100-x}B_x$ with B concentrations between 22 and 85 at.%. The Co/Ta-ratio is constant at 6.8 ± 3.9. T_g increases from 757 ± 1 K to 900 ± 1 K up to a B concentration of 46 at.%, then decreases to around 595 ± 1 K at 59 at.% B, and stays constant around 590 ± 14 K for higher B concentrations. These glass transition temperatures are lower than those reported in literature (T_g = 975 K for $Co_{55}Ta_{10}B_{35}$) [9], which may be attributed to the different synthesis routes.

As T_g is inversely proportional to the configurational entropy S_c [41], S_c is larger for high B concentrations above 59 at.% compared to lower B concentrations. The constant T_g and hence a constant S_c corresponds to a constant number of degrees of freedom for $(Co_{6.8\pm3.9}Ta)_{100-x}B_x$ with more than 59 at.% B, despite the further incorporation of B into the material. This constant number of degrees of freedom suggests the existence of a B network in the high B concentration regime.

Table 1. Glass transition temperature T_g for $(Co_{6.8\pm3.9}Ta)_{100-x}B_x$ as a function of B concentrations determined by high-energy X-ray scattering

Composition (at.%)	T_g in K
$Co_{67}Ta_{11}B_{22}$	757 ± 1
$Co_{56}Ta_{10}B_{34}$	829 ± 1
$Co_{53}Ta_9B_{38}$	899 ± 2
$Co_{46}Ta_8B_{46}$	900 ± 5
$Co_{40}Ta_8B_{52}$	773 ± 1
$Co_{37}Ta_4B_{59}$	595 ± 1
$Co_{35}Ta_4B_{61}$	600 ± 1
$Co_{33}Ta_5B_{62}$	607 ± 1
$Co_{32}Ta_3B_{65}$	-
$Co_{18}Ta_4B_{78}$	573 ± 1
$Co_{12}Ta_3B_{85}$	575 ± 1

3.2. Topology

To further investigate the structural differences with focus on the short-range order, the reduced pair distribution functions G(r) of $(Co_{6.8\pm3.9}Ta)_{100-x}B_x$ as a function of B concentration are shown in Figure 1a. For low B concentrations, the metal-metal (M-M) bonds with a distance of 2.6 Å at 22 at.% dominate G(r). At 3.1 Å, bonds with the second nearest neighbour are visible. The metal-boron (M-B) bonds result in a small peak at 2.1 Å for 22 at.% B, while the B-B bonds are not visible due to the low scattering power of B in X-ray scattering [42].

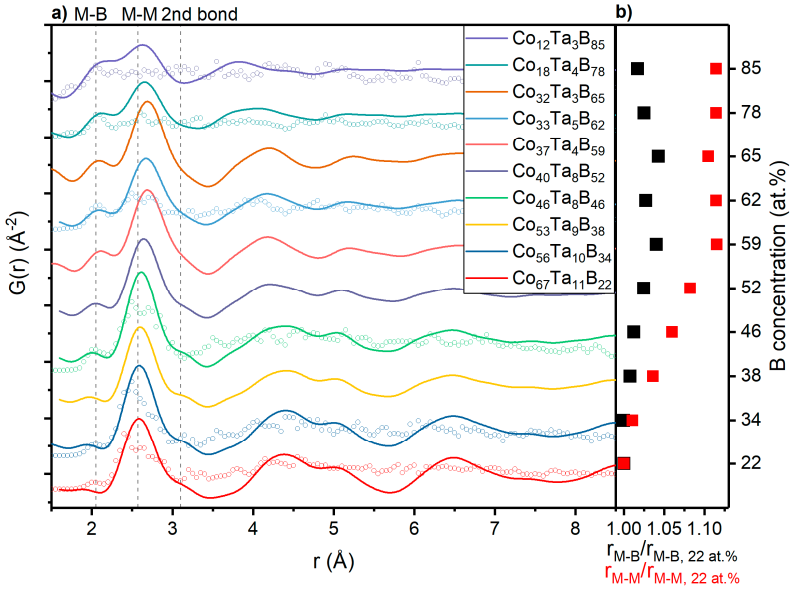

Figure 1. Short range order of $(Co_{6.8\pm3.9}Ta)_{100-x}B_x$. (**a**) Reduced pair distribution functions G(r) for $(Co_{6.8\pm3.9}Ta)_{100-x}B_x$ shown as a function of B concentration obtained by high-energy X-ray scattering. Open circles depict the ab initio G(r) (**b**) Shift of the first and second peak distances r_{M-B}, r_{M-M} of G(r) corresponding to the metal-boron (M-B) and metal-metal (M-M) bonds, respectively. The shift is relative to the peak position for the sample with a B concentration of 22 at.%.

With increasing B concentration, the intensity of the M-B bonds increases, while the intensity of the M-M peak decreases as it is expected for larger B concentrations and the corresponding lower metal concentrations in the sample. Hence, as the B concentration is increased, the metal atoms bond more often with B than with each other. Moreover, the bond lengths r_{M-B} and r_{M-M} increase with an increasing B concentration (Figure 1b). Between 34 and 59 at.% B, the bond lengths increase by 4% for M-B and by 10% for M-M bonds. Above 59 at.%, r_{M-M} remains constant, while r_{M-B} decreases by 2.3%. This is consistent with the evolution of a B network, surrounding the metal atoms and separating them

at a constant distance once the B network completely evolved at 59 at.% B. Simultaneously, the M-B bond length decreases upon further incorporation of B into the network, as the additional B atoms populate the B network and thereby surround the metal atoms more closely.

This B network evolution notion is supported by the calculated total and partial coordination numbers (CN). The total CN (Figure 2a) remains constant around 12 up to 40 at.% B, then decreases between 40 and 70 at.% B down to 10 and stays constant at 7 for B concentrations larger 77 at.%. The low total CN above 77 at.% B is consistent with the formation of a B network structure. Further evidence for the B network evolution is given by the B concentration induced changes in partial CNs. Focusing on the metal coordination in Figure 2b,c, a continuous decrease of metal-metal coordination is observed upon B addition. The decrease of Ta-Co coordination occurs predominantly between 40 and 70 at.%. B. Above 70 at.% B, the metal-metal CN is 0, since the metal-metal bonds are no longer formed and all remaining metal atoms form metal-B bonds. The opposite is observed for the metal-B coordination that increases from 0 to 9 for Co-B and from 0 to 10 for Ta-B in the composition range of 2 to 70 at.% B, being constant at 9 (Co-B) for larger B concentrations. The Ta-B CN above 70 at.% B scatters strongly, as only 3, 2 and 1 Ta atoms are present in the simulation cells for 77, 83, and 92 at.% B, respectively. Hence, these CN may not be significant due to lack of statistics. Finally, the B concentration induced changes in the B-B CN (Figure 2d) give the strongest evidence for the formation of a B network. While the CN for B-B ranges from 0 to 1 for B concentrations lower 40 at.%, a jump of the B-B CN to 3.5 is observed at 40 at.%, which is consistent with the initiation of the B network formation proposed earlier based on the G(r) data shown in Figure 1a. With further increasing B concentration, the CN increases up to 6 for 92 at.% B. The CN of 6 is close the CN of 5.6 for a perfect icosahedron in a crystalline structure [43]. As an icosahedra-like structure with imperfect icosahedra has been predicted and experimentally verified for the amorphous $Al_{0.75}Y_{0.75}B_{14}$ [13], amorphous B_4C [44], as well as for amorphous B [45,46], the partial coordination numbers obtained here give evidence for the formation of an icosahedra-like B network starting to form at 40 at.% B.

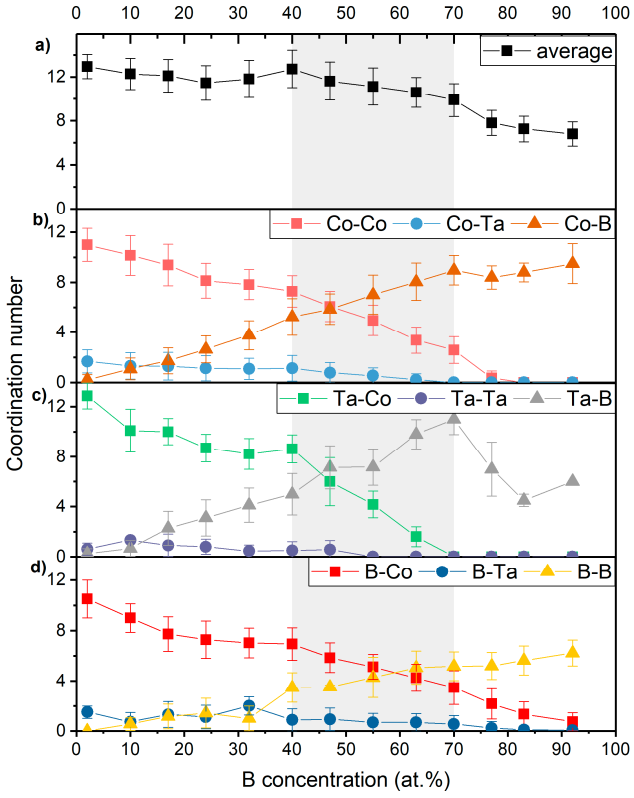

Figure 2. Ab initio coordination number (CN) as a function of B concentration. (**a**) Average CN taking all bonds into account. (**b**–**d**) Partial CN. Lines between the data points serve as a guide to the eye.

Based on the short-range order and topology analysis carried out above, $(Co_{6.8\pm3.9}Ta)_{100-x}B_x$ is identified as metallic glass for B concentrations lower 40 at.% as the metals are predominantly coordinated with metals, while for B concentrations larger 70 at.% a network glass is present due to the presence of an icosahedral-like B network with metal atoms surrounded by B only. Within the concentration range of B concentrations between 40 and 70 at.%, the existence of a glass composite containing metallic glass and covalent glass-like regions is proposed, as the B network evolves in this region and the metal atoms are still coordinated with metals.

To compare physical and in-silico samples, G(r) of the ab initio models are depicted in Figure 1a with open symbols. As the ab initio model can only cover the first coordination shell, bond distances smaller than 3.5 Å should be considered in the ab initio G(r). In the first coordination shell, however, the calculated G(r) exhibits peaks at the M-B, M-M and 2nd bond peak position of the experimentally obtained G(r). It is evident that the M-M peak splits into two peaks, indicating the presence of Co-Co and Co-Ta bonds. For large B concentrations, only the M-B are visible due to the low number of metal atoms in the cell. Considering the small cell size and the associated statistical limitations of the ab initio G(r), the ab initio configurations are consistent with the experiment. However, in contrast to the experimental G(r), also the B-B bonds at 1.71 Å for large B concentrations can be analysed. The B-B bond distances are consistent with icosahedral bonding, as reported in [13,44,46].

To examine the medium-range order (MRO), the structure factor S(q) of $(Co_{6.8\pm3.9}Ta)_{100-x}B_x$ as a function of B concentration is shown in Figure 3a. The S(q) shows clearly that samples are amorphous over the whole compositional range since Bragg peaks are absent. With increasing B concentration up to 62 at.% (Figure 3b), the amorphous principal peak of the structure factor at 3.1 $Å^{-1}$ shows a significant increase in full width at half maximum (FWHM), indicating the formation of less medium range ordered material. This observation is consistent with the higher configurational entropy notion at these B concentrations discussed in the context of the B concentration induced changes in glass transition temperature above. The vanishing double peak at 5.2 and 6.0 $Å^{-1}$ between 22 and 59 at.% B underlines this enhanced disorder. In addition, a shoulder to the principal peak arises at 2.3 $Å^{-1}$ and is clearly visible for B concentrations between 59 and 78 at.%, where the width of the principle peak increases strongly. The onset of the shoulder can already be seen in the asymmetry of the peak at 46 at.% B. This shoulder indicates that two types of medium-range order are present, being consistent with the glass composite regime proposed above.

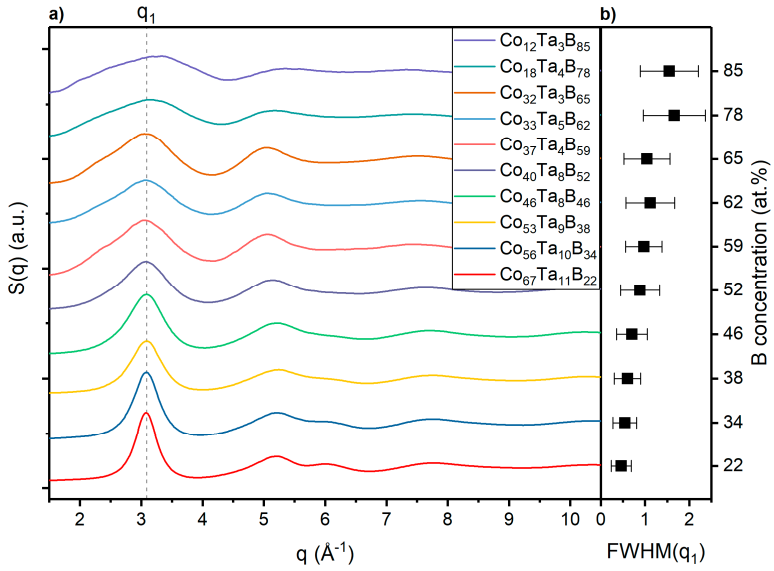

Figure 3. Medium range order of $(Co_{6.8\pm3.9}Ta)_{100-x}B_x$. (**a**) Structure factor S(q) for $(Co_{6.8\pm3.9}Ta)_{100-x}B_x$ shown as a function of B concentration obtained by high-energy X-ray scattering. (**b**) Full width at half maximum (FWHM) of the principal peak q_1 of S(q).

3.3. Electronic Structure

In the next step, we critically appraise the glass composite formation notion by analysis of the electronic structure. According to the free electron model of Nagel and Tauc [47], twice the Fermi vector k_f, which describes the Fermi sphere in amorphous materials, corresponds to the principal peak position of the structure factor q_p in a stable metallic glass:

$$2k_f = q_p \tag{1}$$

Hence, the Fermi level E_f can be experimentally determined from S(q) by inserting Equation (1) into Equation (2) [48]

$$E_f = \frac{\hbar^2}{2m} k_f^2 \tag{2}$$

where $\hbar$ is the Planck constant divided by 2π and m the electron mass. As a comparison of experimentally and theoretically obtained absolute values of E_f is not possible, the relative shift of E_f as a function of B concentration is compared in Figure 4. Based on ab initio data, E_f is constant up to 63 at.% B and decreases for higher B concentrations. The experimentally obtained E_f based on the free-electron model for metallic glasses [47] remains constant for less than 62 at.% B and shifts to larger values for higher B concentrations. This deviation between the free electron model and the ab initio model indicates that the free-electron model is not applicable for B concentrations larger 62 at.%. Hence, the metallic character of the material is lost. This loss of metallic bonding character for B concentrations larger than 62 at.% is consistent with the proposal of a covalent network glass for large B concentrations made above.

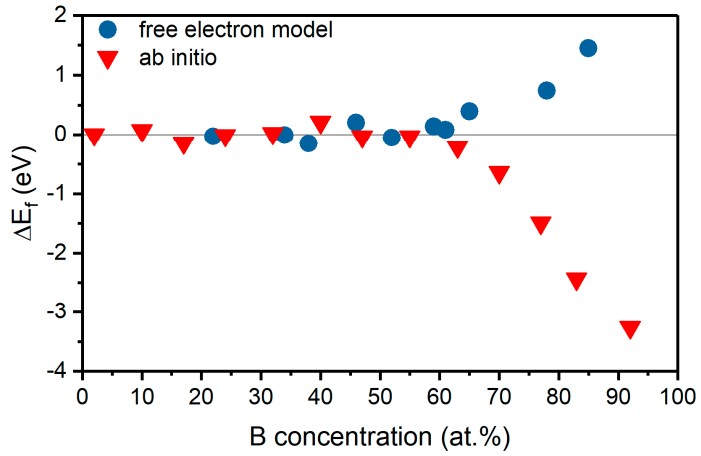

Figure 4. Shift of Fermi level E_f as a function of B concentration. Red triangles are based on the Fermi level calculated by ab initio calculations, the blue circles represent experimental data points based on the free-electron model [47].

The orbital overlap and bond strength give further insight into the change from metallic to covalent character by means of the integrated crystal orbital overlap population (ICOOP) [26] and integrated crystal orbital Hamilton population (ICOHP) [27] at E_f. The latter is a measure of bond strength [28]. Figure 5a plots the partial ICOHP at E_f for Co-B, B-B, Co-Co and Ta-B bonds. While the Co-Co contribution to the bond strength is low and constant up to 77 at.% (for higher B concentrations, Co-Co interaction cannot be found), the metal-B bond strength is between 1.5 and 2 eV, decreasing up to 32 at.% B and staying roughly constant for more than 32 at.% B. Significant changes are observed for the

B-B bond strengths: Up to 32 at.%, the bonding contribution decreases down to −2.9 eV. Subsequently, the bond strength increases further up to –4.8 eV at 77 at.% and is constant for larger B concentrations (negative values are bonding, positive values anti-bonding contributions). The orbital overlap as quantified by ICOOP at E_f (Figure 5b) is consistent with the ICOHP.

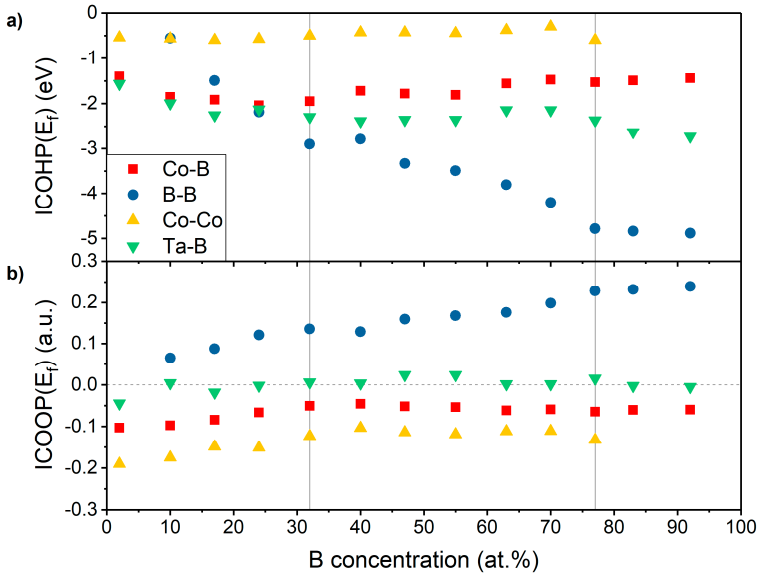

Figure 5. Ab initio bonding analysis of $(Co_{6.8\pm3.9}Ta)_{100-x}B_x$. (**a**) Integrated crystal orbital Hamilton population at the Fermi level (ICOHP(E_f)) and (**b**) integrated crystal orbital overlap population at the Fermi level (ICOOP(E_f)) as a function of B concentration.

Summarizing the ab initio bonding analysis, the change of bonding from metal-metal to metal-B and B-B interactions is driven by increasing B-B bond strength and orbital overlap. Both the measure of bond strength ICOHP(E_f) and the integrated orbital overlap at E_f of B-B as a function of B concentration change slope two times at 32 at.% B and at 77 at.% B, being consistent with the metallic glass, composite, and B network glass regions defined above. The constant bond strength and overlap for B concentrations larger 77 at.% are consistent with the notion of a completely evolved B network in this composition range.

Investigating the B concentration induced changes in binding energy experimentally (Figure 6), the results obtained by XPS are more complex to interpret. For samples with 16, 47 and 65 at.% B, the B 1s binding energy (Figure 6a) exhibits a small but significant peak shift of 0.3 eV to larger binding energies consistent with the ab initio bonding analysis. The peak deconvolution indicates oxidation of the sample with 16 at.% B due to the presence of 16 at.% O in the sample. The B 1s peak, however, can neither be attributed to icosahedral nor to octahedral bonding or bonding in a solid solution, as the binding energies for the B 1s peak in the icosahedral $AlMgB_{14}$ structure with 188.2 eV [49], in Co-B bonds with 188.3 eV [50], in Ta-B bonds with 188.7 eV [51] and alpha-B with 188.0 eV [13] are experimentally not resolvable. The B1s binding energy of icosahedrally bonded B in $AlMgB_{14}$ is shown here as an example for B-rich solids.

The Co $2p_{3/2}$ peak (Figure 6b) for samples with 16, 47 and 65 at.% B at a binding energy of 778.3 eV shows the presence of Co-B bonds as this binding energy is in between those for Co-B bonds in CoB (778.2 eV) and Co_2B (778.6 eV) [50]. The observation of Co-B bonds is consistent with the ab initio bonding analysis. As for the B 1s peak, a small but significant peak shift of 0.2 eV towards higher binding energies between 16 and 65 at.% B is observed. A similar shift is obtained for the Ta 4f feature in the binding energy spectrum (not shown). The larger binding energy for the metals indicates an increased B coordination, consistent with the analysis of the coordination number.

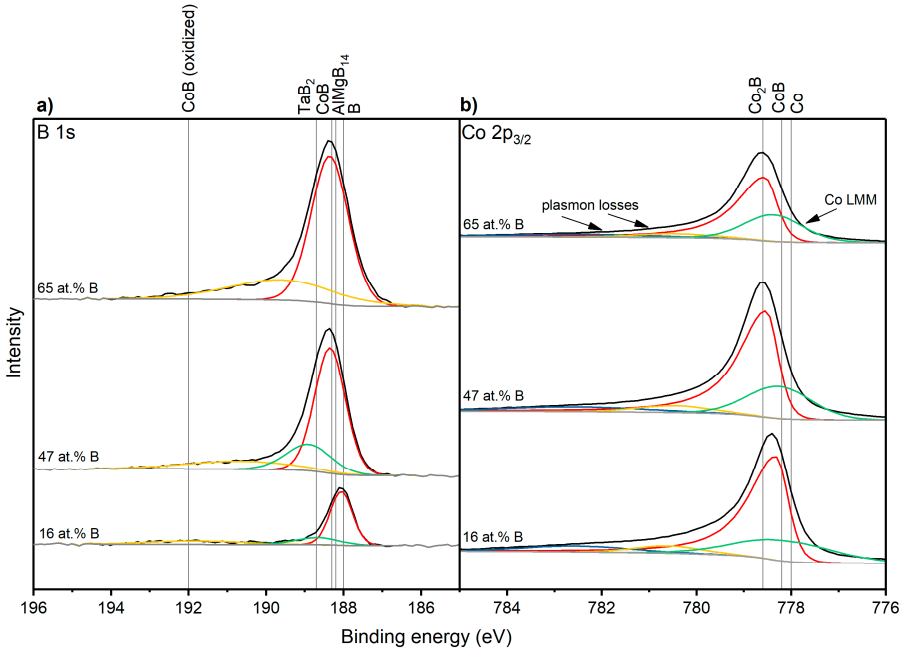

Figure 6. XPS-spectra of $(Co_{6.8\pm3.9}Ta)_{100-x}B_x$. (**a**) B 1s peak and (**b**) Co $2p_{3/2}$ peak. The intensity scale is linear. In black the measured data are shown, in colour the peak deconvolution.

3.4. Magnetization

It is well known that the soft-magnetism of Co-Ta-B is promising to reduce transformer losses [7,10]. Hence, the influence of the enhanced B concentration on the volume magnetization is shown in Figure 7. The total volume magnetization as well as the partial contributions of Co, Ta, and B based on ab initio data are compared with experimental data points of the saturation volume magnetization. The main contribution to volume magnetization comes from Co atoms, while B does not show a magnetic moment. With increasing B concentration, a decrease of magnetization is clearly visible due to the dilution of metal coupling by B. This decrease of magnetization is in agreement with literature [52]. Above 63 at.% B the volume magnetization is approximately 0 due to the lack of metal-metal interactions, explainable by a B network surrounding the metals for high B concentrations. During the decrease from 0.1 to 0 $\mu_B/Å^3$, a change in slope at 40 at.% B is observed, trending with the proposed onset of the region of the glass composite identified above.

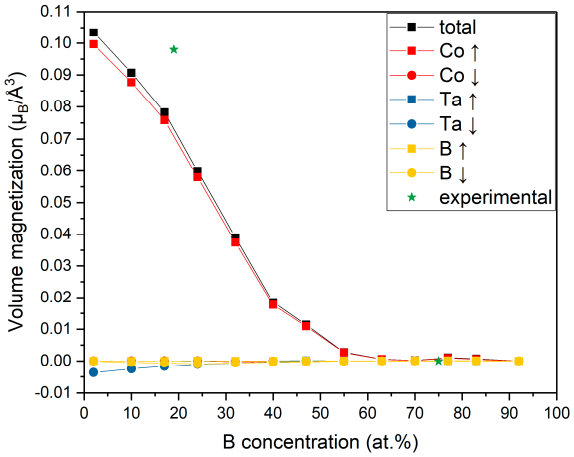

Figure 7. Volume magnetization of $(Co_{6.8\pm3.9}Ta)_{100-x}B_x$ as a function of B concentration based on ab initio calculations. The partial contributions are divided into spin-up and spin-down electrons. Green stars represent experimental values (B concentration 19 and 75 at.%).

Comparing the ab initio volume magnetization with experimental values, the measured near zero saturation magnetization for a sample with 75 at.% B agrees very well with the ab initio data. For a sample with 19 at.% B, the measured saturation volume magnetization of 0.098 $\mu_B/Å^3$ is 25 % larger than the ab initio volume magnetization. This enhanced volume magnetization may be caused by clustering of Co atoms in the physical sample in contrast to the homogenous distribution of Co atoms in the in-silico sample as well as by a different density. This clustering of Co atoms could lead to a phase separation as observed by Kontis et al. [11]. The volume magnetization measurement (Supplementary Figure S2) confirms the soft magnetism reported for the Co-Ta-B system [10].

The B concentration induced transition from a metallic glass to a covalent B network glass has been investigated. It is revealed that these two composition regions are separated by a concentration region where the formation of a glass composite is inferred based on the glass transition temperature T_g, topology, electronic structure, bonding and magnetization. Table 2 summarizes the critical B concentrations for the onset of a B network evolution as well as the beginning of a percolating B network based on each property.

Table 2. Summary of critical B concentrations for the onset and percolation of the B network.

Quantity	Onset B Network Evolution (at.% B)	Onset Percolating B-Network (at.% B)
Glass transition	46	59
Topology	40	70
Free-electron model	-	70
Bonding	32	77
Volume magnetization	40	70

Comparing the critical B concentrations in Table 2, the critical B concentrations for the of onset of the B network evolution and percolation are consistent taking the large variety of quantities and methods as well as the discrete composition changes investigated into account. Hence, we can deduce from the mean concentration values in Table 2 that $(Co_{6.8\pm3.9}Ta)_{100-x}B_x$ is a metallic glass up to a B concentration of 39 ± 5 at.% B. For more than 69 ± 6 at.% B, the material is a network glass dominated by an amorphous icosahedra-like B network.

In between 39 ± 5 and 69 ± 6 at.% B, both metallic bonding and indicators for a B-network are observed. Hence, a glass composite is proposed consisting of metallically bonded regions and B network fragments. As the glass transition temperature changes in this composite regime, a material with defined processability may be designed by controlling the coordination and hence the fraction of icosahedral bonds. Additionally, this glass composite is promising in terms of mechanical properties, as it allows to combine the high strength and stiffness as well as plasticity of metallic glasses with the high stiffness and hardness of the amorphous borides. This combination of mechanical properties in the $(Co_{6.8\pm3.9}Ta)_{100-x}B_x$ system has been reported by Kontis et al. for a self-organized nanostructured material [11]. The self-organized formation of a nanostructure may be enabled by the coexistence of metallic and covalently bonded regions in this concentration range.

4. Conclusions

The B concentration in $(Co_{6.8\pm3.9}Ta)_{100-x}B_x$ was varied systematically from 2 to 92 at% to reveal the composition induced changes in electronic structure and topology in the transition regime between metallic glasses and network glasses. Based on topology and electronic structure, the critical B concentration for the onset of the B network evolution is identified as 39 ± 5 at.%. Below this B concentration the material is a metallic glass. At a B concentration of 69 ± 6 at.% the icosahedral-like B network is percolating the material, enclosing the metal atoms. Hence, the material is a covalent glass in this compositional range. Between 38 ± 5 and 69 ± 6 at.% we reveal the existence of a glass composite that contains metallic regions and B network fragments. We propose that by controlling

the coordination in this glass composite, soft-magnetic amorphous materials with defined plasticity and processability can be designed. Hence, further research should focus on the composition range of 38 ± 5–69 ± 6 at.% B to enable the design of mechanical properties in the range of the glass composite.

Supplementary Materials: The following are available online at http://www.mdpi.com/2410-3896/5/1/18/s1, Supplementary Figure S1: Shift of the principal peak of the structure factor with temperature, Supplementary Figure S2: Hysteresis curve of $Co_{67}Ta_{14}B_{19}$ and $Co_{21}Ta_4B_{75}$ measured at room temperature in a vibrating sample magnetometer

Author Contributions: Conceptualization, S.E. and J.M.S.; methodology, S.E.; formal analysis, S.E., S.P., A.M., M.H., D.P. and A.S.; investigation, S.E., M.H., S.E., D.M.H., L.P. and A.M.; writing—original draft preparation, S.E.; writing—review and editing, S.E., S.P., L.P., A.M., D.M.H., A.S., M.H., D.P., J.M.S.; visualization, S.E.; supervision, A.S. and J.M.S. All authors have read and agreed to the published version of the manuscript.

Funding: This research was funded by Deutsche Forschungsgemeinschaft within the SPP 1594 "Topological Engineering of Ultrastrong Glasses", grant number SCHN 735/22-2). Financial support for the operation of the accelerator laboratory in Uppsala by VR-RFI (contract 821-2012-5144) and the Swedish Foundation for Strategic Research (SSF, contract RIF14-0053) is gratefully acknowledged.

Acknowledgments: Ab initio calculations were performed on the JARA-HPC partition part of the supercomputer CLAIX at RWTH Aachen University within the project JARA0131. Parts of this research were carried out at beamline P02.1 of the light source PETRA III at DESY, a member of the Helmholtz Association (HGF). Access and help to obtain the magnetization data using the PPMS-VSM at JCNS-2/PGI-4, Forschungszentrum Jülich GmbH, is gratefully acknowledged.

Conflicts of Interest: The authors declare no conflict of interest.

References

1. Ashby, M.; Greer, A.L. Metallic glasses as structural materials. *Scripta Mater.* **2006**, *54*, 321–326. [CrossRef]
2. Telford, M. The case for bulk metallic glass. *Mater. Today* **2004**, *7*, 36–43. [CrossRef]
3. Inoue, A.; Shen, B.; Takeuchi, A. Developments and Applications of Bulk Glassy Alloys in Late Transition Metal Base System. *Mater. Trans.* **2006**, *47*, 1275–1285. [CrossRef]
4. Gilman, J.J. Metallic glasses. *Science* **1980**, *208*, 856–861. [CrossRef]
5. Schuh, C.A.; Hufnagel, T.C.; Ramamurty, U. Mechanical behavior of amorphous alloys. *Acta Mater.* **2007**, *55*, 4067–4109. [CrossRef]
6. Greer, A.L. Metallic glasses . . . on the threshold. *Mater. Today* **2009**, *12*, 14–22. [CrossRef]
7. Shen, T.D.; Schwarz, R.B. Bulk ferromagnetic glasses prepared by flux melting and water quenching. *Appl. Phys. Lett.* **1999**, *75*, 49–51. [CrossRef]
8. Wu, Y.; Hui, X.D.; Lu, Z.P.; Liu, Z.Y.; Liang, L.; Chen, G.L. Effects of metalloid elements on the glass-forming ability of Fe-based alloys. *J. Alloy. Compd.* **2009**, *467*, 187–190. [CrossRef]
9. Wang, J.; Li, R.; Hua, N.; Zhang, T. Co-based ternary bulk metallic glasses with ultrahigh strength and plasticity. *J. Mater. Res.* **2011**, *26*, 2072–2079. [CrossRef]
10. Inoue, A.; Shen, B.L.; Koshiba, H.; Kato, H.; Yavari, A.R. Ultra-high strength above 5000 MPa and soft magnetic properties of Co-Fe-Ta-B bulk glassy alloys. *Acta Mater.* **2004**, *52*, 1631–1637. [CrossRef]
11. Kontis, P.; Köhler, M.; Evertz, S.; Chen, Y.-T.; Schnabel, V.; Soler, R.; Bednarick, J.; Kirchlechner, C.; Dehm, G.; Raabe, D.; et al. Nano-laminated thin film metallic glass design for outstanding mechanical properties. *Scripta Mater.* **2018**, *155*, 73–77. [CrossRef]
12. Schnabel, V.; Köhler, M.; Music, D.; Bednarcik, J.; Clegg, W.J.; Raabe, D.; Schneider, J.M. Ultra-stiff metallic glasses through bond energy density design. *J. Phys. Condens. Mat.* **2017**, *29*, 265502. [CrossRef]
13. Music, D.; Hensling, F.; Pazur, T.; Bednarcik, J.; Hans, M.; Schnabel, V.; Hostert, C.; Schneider, J.M. Bonding and elastic properties of amorphous AlYB14. *Solid State Commun.* **2013**, *169*, 6–9. [CrossRef]
14. Stock, M.; Molian, P. Femtosecond pulsed laser deposition of amorphous, ultrahard boride thin films. *J. Vac. Sci. Technol. A* **2004**, *22*, 670. [CrossRef]
15. Tian, Y.; Bastawros, A.F.; Lo, C.C.H.; Constant, A.P.; Russell, A.M.; Cook, B.A. Superhard self-lubricating AlMgB14 films for microelectromechanical devices. *Appl. Phys. Lett.* **2003**, *83*, 2781–2783. [CrossRef]
16. Gupta, S.; Patel, N.; Miotello, A.; Kothari, D.C. Cobalt-Boride: An efficient and robust electrocatalyst for Hydrogen Evolution Reaction. *J. Power Sources* **2015**, *279*, 620–625. [CrossRef]
17. Hohenberg, P.; Kohn, W. Inhomogeneous Electron Gas. *Phys. Rev.* **1964**, *136*, B864–B871. [CrossRef]

18. Hostert, C.; Music, D.; Bednarcik, J.; Keckes, J.; Kapaklis, V.; Hjorvarsson, B.; Schneider, J.M. Ab initio molecular dynamics model for density, elastic properties and short range order of Co-Fe-Ta-B metallic glass thin films. *J. Phys. Condens. Mat.* **2011**, *23*, 475401. [CrossRef]
19. Ozaki, T.; Kino, H. Numerical atomic basis orbitals from H to Kr. *Phys. Rev. B* **2004**, *69*, 195113. [CrossRef]
20. Ozaki, T.; Kino, H. Efficient projector expansion for the ab initio LCAO method. *Phys. Rev. B* **2005**, *72*, 45121. [CrossRef]
21. Perdew, J.P.; Burke, K.; Ernzerhof, M. Generalized Gradient Approximation Made Simple. *Phys. Rev. Lett.* **1996**, *77*, 3865–3868. [CrossRef]
22. Kresse, G.; Furthmüller, J. Efficient iterative schemes for ab initio total-energy calculations using a plane-wave basis set. *Phys. Rev. B* **1996**, *54*, 11169–11186. [CrossRef]
23. Kresse, G.; Joubert, D. From ultrasoft pseudopotentials to the projector augmented-wave method. *Phys. Rev. B* **1999**, *59*, 1758–1775. [CrossRef]
24. Blöchl, P.E. Projector augmented-wave method. *Phys. Rev. B* **1994**, *50*, 17953–17979. [CrossRef]
25. Monkhorst, H.J.; Pack, J.D. Special points for Brillouin-zone integrations. *Phys. Rev. B* **1976**, *13*, 5188–5192. [CrossRef]
26. Hoffmann, R. How Chemistry and Physics Meet in the Solid State. *Angew. Chem. Int. Ed. Engl.* **1987**, *26*, 846–878. [CrossRef]
27. Dronskowski, R.; Bloechl, P.E. Crystal orbital Hamilton populations (COHP): Energy-resolved visualization of chemical bonding in solids based on density-functional calculations. *J. Phys. Chem.* **1993**, *97*, 8617–8624. [CrossRef]
28. Deringer, V.L.; Tchougréeff, A.L.; Dronskowski, R. Crystal orbital Hamilton population (COHP) analysis as projected from plane-wave basis sets. *J. Phys. Chem. A* **2011**, *115*, 5461–5466. [CrossRef]
29. Maintz, S.; Deringer, V.L.; Tchougréeff, A.L.; Dronskowski, R. Analytic projection from plane-wave and PAW wavefunctions and application to chemical-bonding analysis in solids. *J. Comput. Chem.* **2013**, *34*, 2557–2567. [CrossRef]
30. Maintz, S.; Deringer, V.L.; Tchougréeff, A.L.; Dronskowski, R. LOBSTER: A tool to extract chemical bonding from plane-wave based DFT. *J. Comput. Chem.* **2016**, *37*, 1030–1035. [CrossRef]
31. Schnabel, V.; Köhler, M.; Evertz, S.; Gamcova, J.; Bednarcik, J.; Music, D.; Raabe, D.; Schneider, J.M. Revealing the relationships between chemistry, topology and stiffness of ultrastrong Co-based metallic glass thin films: A combinatorial approach. *Acta Mater.* **2016**, *107*, 213–219. [CrossRef]
32. Zhang, Y.; Whitlow, H.J.; Winzell, T.; Bubb, I.F.; Sajavaara, T.; Arstila, K.; Keinonen, J. Detection efficiency of time-of-flight energy elastic recoil detection analysis systems. *Nucl. Instrum. Methods Phys. Res. Sect. B Beam Interact. Mater. Atoms* **1999**, *149*, 477–489. [CrossRef]
33. Ström, P.; Petersson, P.; Rubel, M.; Possnert, G. A combined segmented anode gas ionization chamber and time-of-flight detector for heavy ion elastic recoil detection analysis. *Rev. Sci. Instrum.* **2016**, *87*, 103303. [CrossRef]
34. Janson, M.S. *CONTES Instruction Manual*; Uppsala University: Uppsala, Sweden, 2004.
35. Dippel, A.-C.; Liermann, H.-P.; Delitz, J.T.; Walter, P.; Schulte-Schrepping, H.; Seeck, O.H.; Franz, H. Beamline P02.1 at PETRA III for high-resolution and high-energy powder diffraction. *J. Synchrotron. Radiat.* **2015**, *22*, 675–687. [CrossRef]
36. Hammersley, A.P. *FIT2D. An Introduction and Overview*; ESRF Internal Report ESRF97HA02T; European Synchrotron Radiation Source: Grenoble, France, 1997.
37. Hammersley, A.P.; Svensson, S.O.; Thompson, A. Calibration and correction of spatial distortions in 2D detector systems. *Nucl. Instrum. Meth. A* **1994**, *346*, 312–321. [CrossRef]
38. Hammersley, A.P.; Svensson, S.O.; Hanfland, M.; Fitch, A.N.; Hausermann, D. Two-dimensional detector software: From real detector to idealised image or two-theta scan. *High Press. Res.* **1996**, *14*, 235–248. [CrossRef]
39. Juhás, P.; Davis, T.; Farrow, C.L.; Billinge, S.J.L. PDFgetX3: A rapid and highly automatable program for processing powder diffraction data into total scattering pair distribution functions. *J. Appl. Crystallogr.* **2013**, *46*, 560–566. [CrossRef]
40. Biesinger, M.C.; Payne, B.P.; Grosvenor, A.P.; Lau, L.W.M.; Gerson, A.R.; Smart, R.S.C. Resolving surface chemical states in XPS analysis of first row transition metals, oxides and hydroxides: Cr, Mn, Fe, Co and Ni. *Appl. Surf. Sci.* **2011**, *257*, 2717–2730. [CrossRef]

41. Gupta, P.K.; Mauro, J.C. Composition dependence of glass transition temperature and fragility. I. A topological model incorporating temperature-dependent constraints. *J. Chem. Phys.* **2009**, *130*, 94503. [CrossRef]
42. Henke, B.L.; Gullikson, E.M.; Davis, J.C. X-Ray Interactions: Photoabsorption, Scattering, Transmission, and Reflection at E = 50–30,000 eV, Z = 1–92. *At. Data Nucl. Data Tables* **1993**, *54*, 181–342. [CrossRef]
43. Emin, D. Unusual properties of icosahedral boron-rich solids. *J. Solid State Chem.* **2006**, *179*, 2791–2798. [CrossRef]
44. Bao, R.; Chrisey, D.B. Short range order structure of amorphous B_4C boron carbide thin films. *J. Mater. Sci.* **2011**, *46*, 3952–3959. [CrossRef]
45. Lannin, J.S. Rama scattering in amorphous boron. *Solid State Commun.* **1978**, *25*, 363–366. [CrossRef]
46. Delaplane, R.G.; Dahlborg, U.; Howells, W.S.; Lundström, T. A neutron diffraction study of amorphous boron using a pulsed source. *J. Non-Cryst. Solids* **1988**, *106*, 66–69. [CrossRef]
47. Nagel, S.R.; Tauc, J. Nearly-Free-Electron Approach to the Theory of Metallic Glass Alloys. *Phys. Rev. Lett.* **1975**, *35*, 380–383. [CrossRef]
48. Kittel, C.; Hunklinger, S. *Einführung in die Festkörperphysik*, 15th ed.; unveränd. Aufl.; Oldenbourg: München, Germany, 2013; ISBN 978-3-486-59755-4.
49. Higdon, C.; Cook, B.; Harringa, J.; Russell, A.; Goldsmith, J.; Qu, J.; Blau, P. Friction and wear mechanisms in $AlMgB_{14}$-TiB_2 nanocoatings. *Wear* **2011**, *271*, 2111–2115. [CrossRef]
50. Mavel, G.; Escard, J.; Costa, P.; Castaing, J. ESCA surface study of metal borides. *Surf. Sci.* **1973**, *35*, 109–116. [CrossRef]
51. Wang, Y.; Fan, J.; Trenary, M. Surface chemistry of boron oxidation. 1. Reactions of oxygen and water with boron films grown on tantalum(110). *Chem. Mater.* **1993**, *5*, 192–198. [CrossRef]
52. Hasegawa, R.; Ray, R. Magnetization of glassy Co-B alloys. *J. Appl. Phys.* **1979**, *50*, 1586–1588. [CrossRef]